Analytica Chimica Acta 1319 (2024) 342983

Contents lists available at ScienceDirect

Analytica Chimica Acta

journal homepage: www.elsevier.com/locate/aca

Probing rotaxane dynamics with ^{19}F NMR/MRI: Unveiling the roles of mechanical bond and steric hindrance

Yu Li [a,1], Man Luo [a,b,1], Mou Jiang [a,1], Rui Zhou [a,1], Wanrong Yang [b], Shenhui Li [a,c], Fang Wang [a], Lijun Zhu [a], Pei He [a], Minghui Yang [a,c], Xin Zhou [a,c], Zhong-Xing Jiang [a,c,d,*], Shizhen Chen [a,c,**]

[a] State Key Laboratory of Magnetic Resonance and Atomic and Molecular Physics, National Center for Magnetic Resonance in Wuhan, Wuhan Institute of Physics and Mathematics, Innovation Academy for Precision Measurement Science and Technology, Chinese Academy of Sciences-Wuhan National Laboratory for Optoelectronics, Huazhong University of Science and Technology, Wuhan, 430071, China
[b] School of Pharmaceutical Sciences, Wuhan University, Wuhan, 430071, China
[c] University of Chinese Academy of Sciences, Beijing, 100049, China
[d] Key Laboratory of Organofluorine Chemistry, Shanghai Institute of Organic Chemistry, Chinese Academy of Sciences, Shanghai, 200032, China

HIGHLIGHTS

- Synthesized rotaxanes feature sensitive, selective, semi-quantitative ^{1}H/^{19}F NMR reporters for molecular dynamics analysis.
- ^{19}F NMR/MRI offers insights into rotaxanes' structure/dynamics using relaxation rates, rotational correlation time, and imaging features.
- Reveals the interplay between mechanical bonds and steric hindrance in rotaxanes via comparative analysis.

GRAPHICAL ABSTRACT

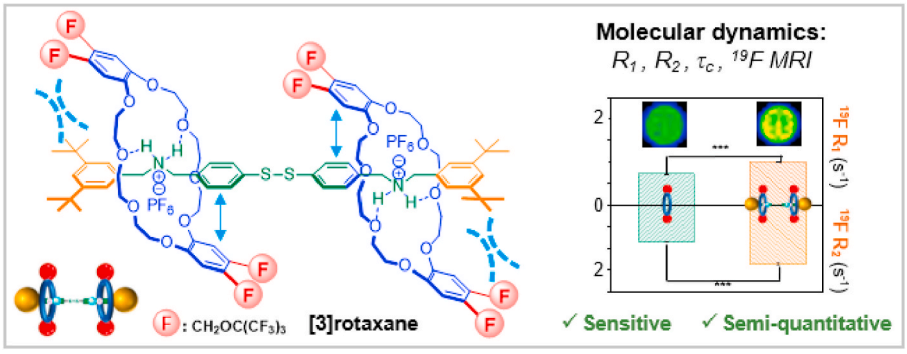

ARTICLE INFO

Keywords:
Rotaxane
Molecular dynamics
^{19}F NMR/MRI

ABSTRACT

Background: Deciphering the molecular dynamics (MD) of rotaxanes is crucial for designing and refining their applications in molecular devices. This study employed fluorine-19 nuclear magnetic resonance (^{19}F NMR) and magnetic resonance imaging (MRI) to unveil the interplay between mechanical bonds and steric hindrance in a series of fluorinated rotaxanes.

* Corresponding author. State Key Laboratory of Magnetic Resonance and Atomic and Molecular Physics, National Center for Magnetic Resonance in Wuhan, Wuhan Institute of Physics and Mathematics, Innovation Academy for Precision Measurement Science and Technology, Chinese Academy of Sciences-Wuhan National Laboratory for Optoelectronics, Huazhong University of Science and Technology, Wuhan, 430071, China.
** Corresponding author. State Key Laboratory of Magnetic Resonance and Atomic and Molecular Physics, National Center for Magnetic Resonance in Wuhan, Wuhan Institute of Physics and Mathematics, Innovation Academy for Precision Measurement Science and Technology, Chinese Academy of Sciences-Wuhan National Laboratory for Optoelectronics, Huazhong University of Science and Technology, Wuhan, 430071, China.
E-mail address: zxjiang@apm.ac.cn (Z.-X. Jiang).
[1] These authors contributed equally to this work.

https://doi.org/10.1016/j.aca.2024.342983
Received 16 April 2024; Received in revised form 10 July 2024; Accepted 14 July 2024
Available online 20 July 2024

Mechanical bond
Steric hindrance

Results: $^{1}H/^{19}F$ NMR revealed stable "Z"-shaped wheel conformations minimizing steric clashes and favoring π-π interactions with the axle. Utilizing fluorines and axle protons as reporters, $^{1}H/^{19}F$ relaxation rates and solid-state ^{19}F NMR studies demonstrated that mechanical bond primarily governs wheel motion, while steric hindrance dictates axle movement. Intriguingly, mechanical bond mainly affects local axle groups, leaving distant ones minimally impacted. MD simulations corroborated these findings. Temperature-dependent ^{19}F NMR indicated that energy input enhances rotational motion and wheel conformational transitions. Furthermore, the drastic increase in ^{19}F relaxation rates upon mechanical bond formation and steric hindrance enables sensitive and selective ^{19}F MRI visualization of MD changes.
Significance: This study, by elucidating the roles of internal and external factors on rotaxane molecular dynamics using ^{19}F NMR/MRI, offers valuable insights that can advance the field of rotaxane-based molecular devices.

1. Introduction

Rotaxanes, intricate molecules characterized by cyclic wheel molecules threaded onto axle molecules and capped by bulky stoppers, have undergone significant development as versatile molecular devices [1–7]. A mechanical bond is a distinctive type of chemical bond observed in rotaxanes, which refers to the spatial entanglement between two or more molecular entities [8]. To emulate real-world devices, rotaxanes are often engineered to execute intramolecular motions facilitated by mechanical bonds, including stationing, rotation, and shuttling along the axle. Understanding the molecular dynamics (MD) of rotaxanes is crucial for the rational design and innovative applications of rotaxane-based molecular devices [9–11]. For instance, in our daily lives, these interlocked "axle-wheel" structures are predominantly utilized as spinning devices rather than shuttling devices, as seen in applications like steering wheels and Ferris wheels. However, the study of rotaxanes as spinning devices remains scarce, likely due to the challenges associated with monitoring their MD. Regrettably, only a handful of analytical techniques exist for investigating the MD of rotaxanes, such as ^{1}H NMR, X-ray diffraction, and molecular dynamics simulations [12–16]. Hence, there is an urgent demand for novel strategies to monitor MD, particularly regarding spin motion.

Given that the NMR signal of a spin nucleus is profoundly influenced by its environment and dynamics, the NMR signal of a reporter group within a rotaxane can offer a sensitive reflection of its molecular dynamics [17–19]. Among the various spin nuclei, ^{19}F holds significant advantages for monitoring rotaxanes. It ranks as the second most sensitive nucleus for NMR, boasts stable nuclei with 100 % natural abundance, features a broad (approximately 400 ppm) and environment-sensitive chemical shift, and exhibits no background signal in regular systems [20–22]. Thus, fluorination of rotaxanes can facilitate convenient studies of molecular dynamics using ^{19}F NMR. However, despite these advantages, only a limited number of fluorinated rotaxanes have been reported to date [23–26]. Recently, we developed a fluorinated pinwheel [2]rotaxane ($\mathbf{R_F}$) as a sensitive ^{19}F MRI agent, wherein the mechanical bond was leveraged to shorten the ^{19}F relaxation times and enhance the ^{19}F MRI sensitivity (Scheme 1) [26]. The 36 fluorines in the wheel of $\mathbf{R_F}$ produced a distinct singlet peak devoid of background signals, serving as sensitive and selective reporters of molecular dynamics within the wheel component. Meanwhile, although the protons in rotaxanes yield multiple congested ^{1}H NMR peaks within a chemical shift range of less than 10 ppm, the 36 *tert*-butyl protons generate a ^{1}H NMR peak characterized by the strongest intensity and a distinctive chemical shift, providing insights into the dynamics of the axle. By leveraging the information from $^{1}H/^{19}F$ NMR, the molecular dynamics of rotaxanes can be vividly depicted.

In this study, we synthesized a series of fluorinated rotaxanes and employed the multiple magnetically equivalent fluorines as sensitive ^{19}F NMR/MRI reporters to comparatively investigate the influence of mechanical bonds, steric hindrance, and molecular weight on MD (Scheme 1). By examining [2]rotaxanes $\mathbf{R_F}$, $\mathbf{R_{2F}}$, and [3]rotaxane $\mathbf{R_{3F}}$ (the axle plus wheel) in succession, we observed a gradual increase in steric hindrance of the MD reporter, providing an ideal comparative model to explore the impact of steric hindrance on rotaxane MD using $^{1}H/^{19}F$ NMR. Moreover, in comparison to the wheel motion observed in [2]rotaxanes $\mathbf{R_F}$ and $\mathbf{R_{2F}}$, the presence of double wheels and a relatively

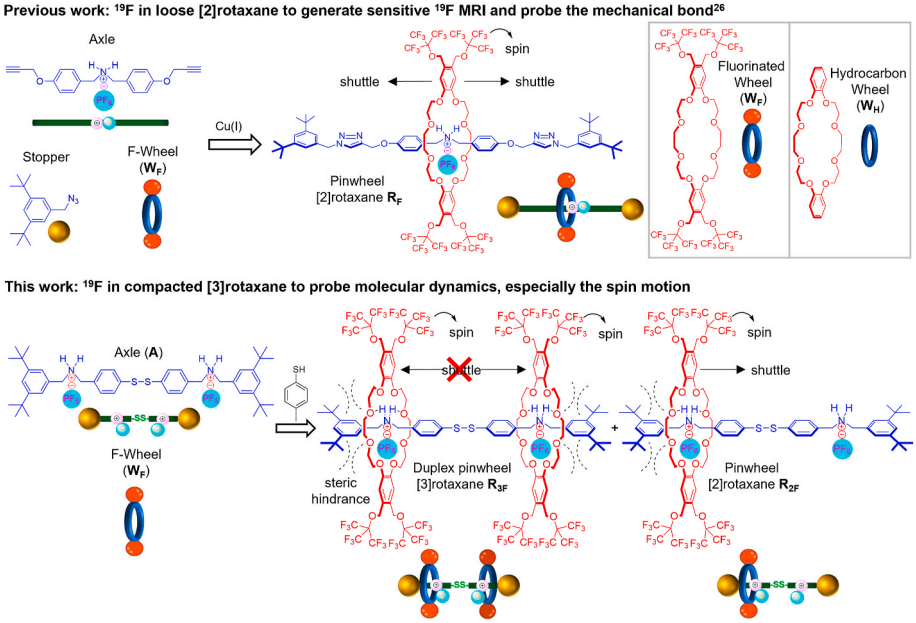

Scheme 1. Design of fluorinated rotaxanes $\mathbf{R_F}$, $\mathbf{R_{2F}}$, and $\mathbf{R_{3F}}$ and their ^{19}F NMR/MRI-based MD study.

short axle in $\mathbf{R_{3F}}$ substantially constrained shuttling and conformational transitions of the wheel, thus offering a model for investigating spin motion in rotaxanes. In these comparative models, factors influencing rotaxane MD were semi-quantitatively reflected by changes in the reporters' relaxation rates (ΔR) and directly visualized by ^{19}F MRI signal intensity. Concurrently, molecular dynamics simulations provided detailed insights into the structure and MD of the rotaxanes, confirming and complementing the findings from ^{19}F NMR/MRI experiments. A comprehensive understanding of MD in rotaxanes and its key influencing factors holds the potential to advance the development of molecular devices, including improved shuttling devices and novel spin devices.

2. Materials and methods

2.1. General

Dibenzo 24-crown-8 was purchased from Bidepharm (Shanghai, China), paraformaldehyde and sodium borohydride were purchased from Energy Chemical (Anhui, China), triphenylphosphine and 3-chloroperoxybenzoic acid were purchased from Adamas-beta (Shanghai, China). ^{1}H, ^{13}C and ^{19}F NMR spectra were recorded on a Bruker 400 MHz or 500 MHz spectrometer. High-resolution mass spectra (HRMS) were recorded on a Thermo Fisher Scientific Q Exactive Focus. MALDI-ICR mass spectra were recorded on a 9.4 T SolariX FT-ICR-MS using the single MS mode for positive ions with dithranol as a matrix.

2.2. Synthesis of rotaxanes R_{2F} and R_{3F}

Wheel $\mathbf{W_F}$ (400 mg, 0.28 mmol) and Axle **A** (100 mg, 0.10 mmol) were dissolved in DCM (3 mL), and *p*-toluenethiol (1 mg, 0.01 mmol) was added to the solution. The reaction mixture was stirred overnight at room temperature. After removal of the solvent under reduced pressure, the residue was purified by flash column chromatography on silica gel (DCM:MeOH = 20:1) to give [3]Rotaxane $\mathbf{R_{3F}}$ and [2]Rotaxane $\mathbf{R_{2F}}$ as white solids ($\mathbf{R_{3F}}$: 183 mg, yield 46 %; $\mathbf{R_{2F}}$: 36 mg, yield 15 %). Note: A higher yield of $\mathbf{R_{2F}}$ (100 mg, yield 40 %) could be obtained when 1.0 equivalent of $\mathbf{W_F}$ (150 mg, 0.10 mmol) was applied.

2.3. Variable temperature ^{19}F MAS NMR

Variable temperature ^{19}F MAS NMR experiments were carried out on a Bruker Avance 400 MHz spectrometer with a 4.0 mm double-resonance MAS probe. The Larmor frequency is 375.7 MHz for ^{19}F. ^{19}F MAS NMR spectra were acquired with a π/2 pulse length of 5.0 μs and a recycle delay of 5 s. The T_1 relaxation time of various protons was measured using the inversion–recovery method. ^{19}F NMR chemical shift was externally referenced to trifluoroacetic acid.

2.4. Molecular dynamics simulations

The systems for MD simulations were built by placing each of the rotaxanes in the center of a cubic box with a volume of 60 × 60 × 60 Å^3 containing 4000 acetonitrile molecules. The axle conformation was generated by quantum chemical calculations with PM6 method performed on Gaussian09 software. The modeling systems were built by PyMol and PackMol program. MD simulations were performed by AMBER18 software package supported GPU computation with the CUDA version of pmemd program. Each of the modeling systems was carried out 4 independent trajectories with conventional simulation steps of minimization, and equilibration before MD production. During the equilibration processes, the systems were heated in constant volume (NVT ensemble) and equilibrated in constant pressure (NPT ensemble) conditions. After 10 ns of equilibration, the production MD simulations were performed for 100 ns under the constant pressure of 1.0 bar using Berendsen barostat at 300K. Time step was set to 1fs and every 10 ps saved one snapshot.

2.5. ^{19}F MRI phantom experiments of W_F, R_{2F}, and R_{3F}

^{19}F MRI phantom experiments were performed on a Bruker BioSpec 9.4 T MRI system. The temperature of the magnet room was maintained at 24 °C during the experiment. The ^{19}F phantom images were acquired using a RARE pulse sequence, RARE factor = 4, matrix size = 32 × 32, slice thickness = 20 mm, FOV = 3.0 cm × 3.0 cm, TR = 600 ms, TE = 17.5 ms, scan time = 307 s.

2.6. Statistical analysis

The analyzed data are presented as mean ± standard deviation of n = 3 replicates. Statistical significance was assessed by unpaired two-tailed Student's t-test.

3. Results and discussion

Initially, rotaxanes $\mathbf{R_{2F}}$, $\mathbf{R_{3F}}$, and $\mathbf{R_{3H}}$ were synthesized, as depicted in Scheme 2. The fluorinated wheel $\mathbf{W_F}$ and [2]rotaxane $\mathbf{R_F}$ were prepared utilizing our previously established method [26], while the axle **A** was synthesized following a published protocol [27]. Employing *p*-thiocresol as the initiator, the disulfide exchange "unlock-lock" process involving **A** and $\mathbf{W_F}$ yielded [3]rotaxane $\mathbf{R_{3F}}$ with a 46 % yield on a 0.8-g scale, alongside a minor amount of [2]rotaxane $\mathbf{R_{2F}}$ with a 15 % yield. Similarly, the non-fluorinated [3]rotaxane $\mathbf{R_{3H}}$ was obtained from **A** and $\mathbf{W_H}$ with a 55 % yield, serving as a reference standard. High purities of $\mathbf{R_{3F}}$ and $\mathbf{R_{2F}}$ were confirmed via HPLC analysis (Fig. S1), with the formation of rotaxanes corroborated by the presence of cation peaks in their Maldi-Tof mass spectra (see Supporting Information). Noteworthy is the disulfide-exchange assembly method employed for $\mathbf{R_{3F}}$, which circumvents the use of copper-catalyzed azide-alkyne cycloaddition [28]. This approach mitigates the potential interference caused by paramagnetic copper, which, if not thoroughly removed, could significantly alter the longitudinal and transverse relaxation rates (R_1 and R_2) of the nuclei, thereby complicating molecular dynamics studies using ^{1}H/^{19}F NMR [29].

The densely packed structure of [3]rotaxane $\mathbf{R_{3F}}$ was thoroughly examined using 1D and 2D ^{1}H/^{19}F NMR spectra (Fig. 1a and S2). Compared with the reference axle **A**, the noticeable downfield shifts of axle protons H_e (0.64 ppm) and H_f (0.30 ppm) in the ^{1}H NMR spectrum of $\mathbf{R_{3F}}$ were observed, likely resulting from the deshielding effects of hydrogen bonds (Fig. 1b), indicating the positioning of the wheels on the positively charged amine of the axle [30]. Conversely, the upfield shifts observed for axle protons H_a (−0.44 ppm), H_c (−0.40 ppm), and wheel proton H_A (−0.14 ppm) implied a π-π interaction between phenyl groups I and II in $\mathbf{R_{3F}}$, induced by the ring-current shielding effect [31]. Additionally, the distinct signal splitting observed in H_C, H_D, and H_E of $\mathbf{R_{3F}}$ (Fig. 1b) indicates an asymmetry structure of the molecule. This signal splitting likely arises from the constrained conformational transition of the wheel, which breaks the magnetic equivalence of the corresponding protons. Furthermore, the marginal upfield shifts observed for axle protons H_b (−0.16 ppm) and H_d (−0.08 ppm) indicated a delicate π-π interaction between phenyl groups III and IV in $\mathbf{R_{3F}}$, potentially influenced by the pronounced steric hindrance between the perfluoro-*tert*-butyl and *tert*-butyl groups. Analysis of the ^{1}H–^{1}H rotational-frame Overhauser effect spectroscopy (ROESY) NMR spectrum of $\mathbf{R_{3F}}$ revealed cross-peaks between H_C, H_D, H_E, and H_d, indicating the proximity of the crown ether and phenyl group III (Fig. 1c). Conversely, the significantly larger downfield shift observed for axle protons H_e (0.64 ppm) compared to H_f (0.30 ppm) in the ^{1}H NMR spectra, the absence of cross-peaks between H_C, H_D, H_E, and H_a in the ^{1}H–^{1}H ROESY NMR spectrum, and the presence of cross-peaks between the perfluoro-*tert*-butyl fluorines and *tert*-butyl H_g in the ^{1}H–^{19}F HOESY NMR spectrum (Fig. 1d) indicated the crown ether's closer proximity to

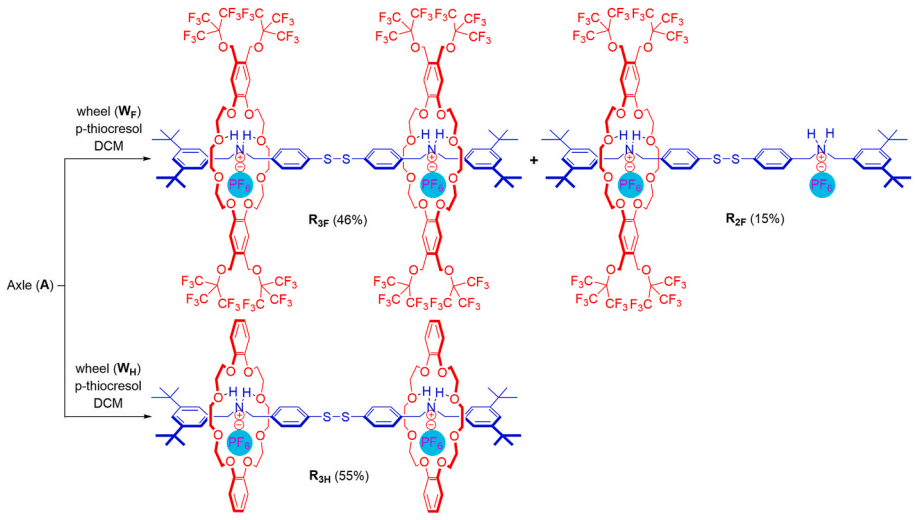

Scheme 2. Synthesis of rotaxanes $\mathbf{R_{2F}}$, $\mathbf{R_{3F}}$, and $\mathbf{R_{3H}}$.

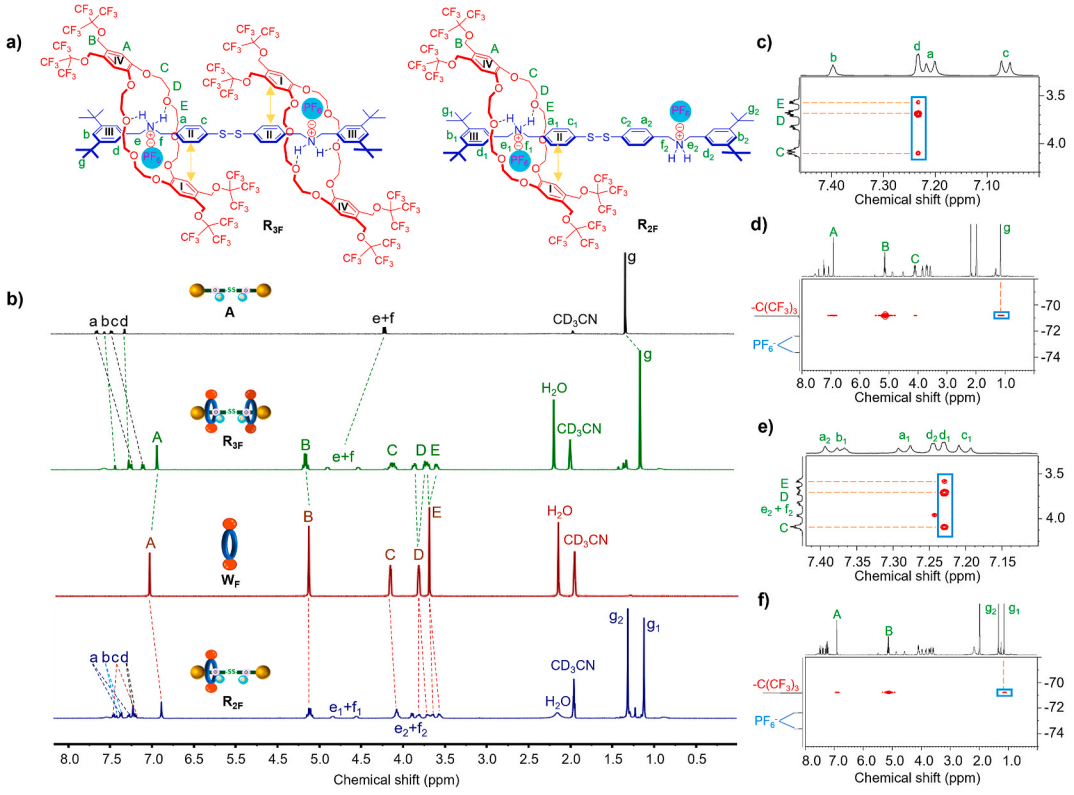

Fig. 1. Proposed stable conformations of $\mathbf{R_{3F}}$ and $\mathbf{R_{2F}}$ with labeled protons and phenyl groups (a). Partial ^{1}H NMR spectra of **A**, $\mathbf{R_{3F}}$, $\mathbf{W_F}$, and $\mathbf{R_{2F}}$. The expanded views of 7.8-7.0 ppm and 5.0–3.0 ppm regions can be found in the supporting information (b). ^{1}H–^{1}H ROESY NMR spectra of $\mathbf{R_{3F}}$ (c) and $\mathbf{R_{2F}}$ (e). ^{1}H–^{19}F HOESY NMR spectra of $\mathbf{R_{3F}}$ (d) and $\mathbf{R_{2F}}$ (f). NMR conditions: 2.5 mM in CD_3CN at 298 K, 500 MHz for 1D NMR, and 600 MHz for 2D NMR.

phenyl group III than phenyl group II, with the perfluoro-*tert*-butyl groups positioned adjacent to the *tert*-butyl groups, thereby alleviating steric hindrance in the phenyl group II region. Moreover, cross-peaks observed between H_a, H_c, and H_A in the ^{1}H–^{1}H ROESY NMR spectrum (Fig. S3) provided further evidence of a π-π interaction between phenyl groups I and II. These findings collectively pointed to a twisted "Z" conformation of the wheel, characterized by a robust π-π interaction between phenyl groups I and II, a weaker interaction between phenyl groups III and IV, and the extension of perfluoro-*tert*-butyl groups toward the *tert*-butyl groups, resulting in a "double-wave" shaped $\mathbf{R_{3F}}$ structure aimed at accommodating bulky groups and minimizing steric hindrance (Fig. 1a).

The intricate structure of [3]rotaxane $\mathbf{R_{3F}}$ was further scrutinized in comparison with less densely packed rotaxanes $\mathbf{R_F}$, $\mathbf{R_{2F}}$, and $\mathbf{R_{3H}}$, aiming to elucidate the underlying steric effects. Comparable π-π interactions and a twisted "Z" conformation were also discerned in the crystal structure of $\mathbf{R_F}$, as reported previously [26], while no discernible signal splitting of the crown ether protons was evident in its ^{1}H NMR spectrum. This absence suggested that the relatively elongated axle and the distantly located *tert*-butyl groups facilitated a smooth conformational transition of the wheel. Despite possessing a shorter axle and adjacent *tert*-butyl groups, $\mathbf{R_{2F}}$ exhibited similar π-π interactions and a twisted "Z"

conformation of the wheel (Fig. 1b, 1e, and 1f), as observed in **R_F**. However, the constrained conformational transition of the wheel was affirmed by the presence of split H_C, H_D, and H_E peaks in the ^{1}H NMR spectrum of **R_{2F}**. In comparison to **R_F**, the impeded conformational transition of the wheel in **R_{2F}** and **R_{3F}** likely stems from steric hindrance between the bulky perfluoro-*tert*-butyl and *tert*-butyl groups. Notably, in the absence of the perfluoro-*tert*-butyl group, **R_{3H}** also displayed analogous split crown ether proton peaks (Fig. S4), indicating that the hindrance to the wheel's conformational transition is primarily influenced by the adjacent *tert*-butyl groups, given their proximity to the positively charged amine. These observations collectively suggest that the bulky perfluoro-*tert*-butyl and *tert*-butyl groups exert a significant influence on the MD of the rotaxanes, diminishing the π-π interaction and retarding the wheel's conformational transition.

Following the elucidation of stable conformations, the MD of rotaxanes **R_F**, **R_{2F}**, and **R_{3F}** were comprehensively investigated using ^{1}H/^{19}F relaxation rates as MD indicators. Assessing the wheel's perspective, we measured the relaxation rates of the wheel fluorines in the rotaxanes and calculated their changes relative to wheel **W_F** ($\Delta R = [R\ (\mathbf{R_{Rtx}})\text{-}R\ (\mathbf{W_F})]/R\ (\mathbf{W_F})\times 100$ %, as shown in Fig. 2a). Incorporation of **W_F** into the rotaxanes resulted in significant relaxation rate increases in the wheel fluorines (**R_F**: $\Delta R_1 = 27$ %, $\Delta R_2 = 38$ %; **R_{2F}**: $\Delta R_1 = 33$ %, $\Delta R_2 = 42$ %; **R_{3F}**: $\Delta R_1 = 38$ %, $\Delta R_2 = 59$ %), suggesting that the formation of mechanical bond and hydrogen bonding substantially restricted the motion of the wheel. Notably, the larger relaxation rate increases observed in **R_{2F}** compared to **R_F**, despite their similar chemical environments, implied that the wheel motion was hindered by the adjacent bulky *tert*-butyl groups. Moreover, with an additional wheel, **R_{3F}** exhibited even greater relaxation rate increases than **R_{2F}** ($\Delta R_1 = 4$ %, $\Delta R_2 = 11$ %), indicating further hindrance to wheel motion due to steric hindrance between the perfluoro-*tert*-butyl groups. However, the increase in relaxation rates is not as pronounced. Thus, the motion of the wheels in the rotaxanes was predominantly governed by mechanical bonds and modulated by the steric hindrance of the *tert*-butyl and perfluoro-*tert*-butyl groups.

From the axle perspective, we compared the relaxation rates of stopper *tert*-butyl protons H_g in the rotaxanes and in axle **A** (Fig. 2b). In contrast to **A**, the formation of rotaxane **R_F** resulted in moderate relaxation rate increases in proton H_g ($\Delta R_1 = 13$ %, $\Delta R_2 = 11$ %). For the more crowded and asymmetric **R_{2F}**, the crowded wheel side proton H_{g1} exhibited significant relaxation rate increases ($\Delta R_1 = 86$ %, $\Delta R_2 = 109$ %), while the loose side H_{g2} displayed minimal increase in R_1 ($\Delta R_1 = 1$ %) and a notable increase in R_2 ($\Delta R_2 = 36$ %). Notably, the relaxation rate increases in the axle protons H_g of crowded **R_{3F}** ($\Delta R_1 = 88$ %, $\Delta R_2 = 117$ %) closely resembled those of H_{g1} in **R_{2F}**, particularly in terms of ΔR_1. These observations suggest that the motion of the stopper groups in the axle was primarily influenced by the adjacent wheel, with the influence diminishing with the stopper-wheel distance. Moreover, the significantly different ΔR values of H_{g1} and H_{g2} in **R_{2F}**, and the similar ΔR values of axle protons H_{g1} in **R_{2F}** (2413 Da) and H_g in **R_{3F}** (3845 Da) despite their considerable difference in molecular weight, indicate that molecular weight plays a minor role in the MD of the rotaxanes. Therefore, although residing within the same rotaxanes, the wheel and the axle exhibit distinct MD profiles, likely due to the more rigid cyclic structure of the wheel and the comparatively flexible structure of the axle.

To elucidate the impact of perfluoro-*tert*-butyl groups on MD, we conducted a comparative analysis of relaxation rate changes in corresponding protons within **R_{3F}** and **R_{3H}**. Comparing with **W_F**, wheel protons H_A in **R_{3F}** exhibited notable relaxation rate increases ($\Delta R_1 = 50$ %, $\Delta R_2 = 109$ %), while H_A in **R_{3H}** displayed even greater increases ($\Delta R_1 = 70$ %, $\Delta R_2 = 149$ %). This suggests that the presence of bulky perfluoro-*tert*-butyl groups in **R_{3F}** weakened the π-π interaction and facilitated the motion of H_A (Fig. 2c). Conversely, for axle protons H_g, the trend was reversed, with significantly larger relaxation rate increases observed in **R_{3F}** ($\Delta R_1 = 88$ %, $\Delta R_2 = 117$ %) compared to **R_{3H}** ($\Delta R_1 = 57$ %, $\Delta R_2 =$

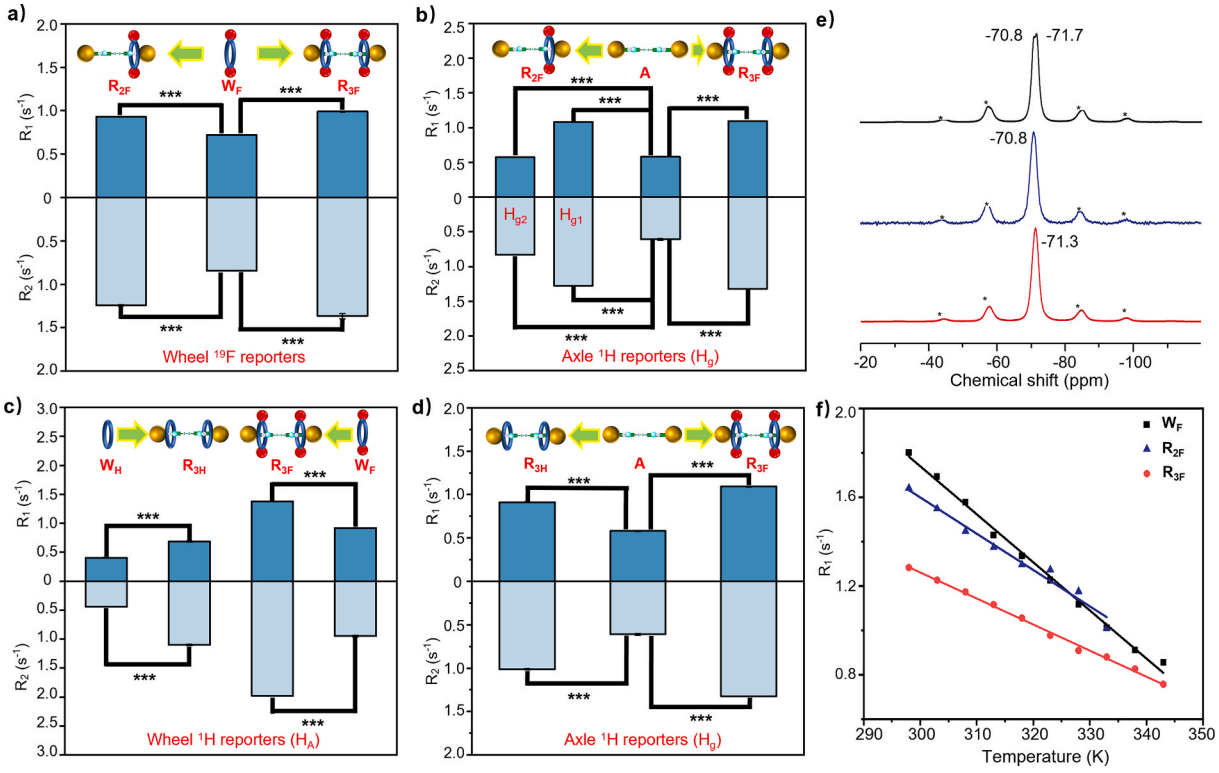

Fig. 2. ^{19}F/^{1}H relaxation rates of the wheel fluorines (a), axle protons H_g (b, d), and wheel protons H_A (c) in **R_{2F}**, **R_{3F}**, **R_{3H}**, and their components. Solid-state ^{19}F MAS NMR spectra (e) and temperature-dependent ^{19}F R_1 (f) of **W_F**, **R_{2F}**, and **R_{3F}**. Statistical significance: ***p < 0.001. NMR conditions: 0.5 mM in CD_3CN at 298 K, 500 MHz for relaxation rate measurement, and 400 MHz for solid-state NMR.

66 %). This disparity likely stems from the steric hindrance between the bulky perfluoro-*tert*-butyl and *tert*-butyl groups (Fig. 2d). Therefore, the comparative relaxation rate analysis highlights how the formation of rotaxanes markedly restricts wheel and adjacent axle group motions through mechanisms such as mechanical bonds, hydrogen bonding, π-π interaction, and steric hindrance, underscoring the sensitivity of relaxation rates as MD indicators. Furthermore, the distinct advantages of the intense, singlet, and background-free ^{19}F signal make it a superior status indicator compared to the crowded, overlapped, and background-interfered ^{1}H signal.

Given the strong dependence of spin nucleus relaxation rates on its rotational motions, particularly internal rotations, solid-state ^{19}F magic angle spinning (MAS) NMR was employed to ascertain the rotational correlation time (τ_c) of the wheel fluorines—an essential parameter in MD. Comparing with $\mathbf{W_F}$, rotaxanes $\mathbf{R_{2F}}$, and $\mathbf{R_{3F}}$ exhibited notable peak broadening in the ^{19}F MAS NMR spectra (Fig. 2e), indicative of interactions between the wheel and the axle. Upon fitting the temperature-dependent ^{19}F R_1 to the Kubo-Tomita equation [32], the τ_c values of $\mathbf{W_F}$, $\mathbf{R_{2F}}$, and $\mathbf{R_{3F}}$ were determined as 0.33 ps, 1.36 ps, and 1.96 ps, respectively (Fig. 2f). These findings underscore a significant slowdown in the internal rotation of fluorines in the sequence of $\mathbf{W_F}$, $\mathbf{R_{2F}}$, and $\mathbf{R_{3F}}$, highlighting the associated steric hindrance and its pronounced impact on the rotational motions of the wheel fluorines.

Additionally, MD simulations were conducted to gain further insight into the behavior of rotaxanes $\mathbf{R_{2F}}$ and $\mathbf{R_{3F}}$ using the AMBER18 software package, with GPU computation supported by the CUDA version of the pmemd program [33]. We calculated the center distances from phenyl group II of the axle to phenyl group I or IV of the wheel. Considering the indistinguishable nature of the π-π stacking interactions between a phenyl group on the axle and one on the wheel due to configuration symmetry, only the minimum distance was considered as the parameter to explore the π-π interactions for each snapshot of the conformation along the simulated trajectories. The simulated results, as illustrated in Fig. 3 and S5, indicate that both $\mathbf{R_{2F}}$ and $\mathbf{R_{3F}}$ favor the formation of π-π interactions, with the minimum π-π distance of simulated conformations consistently below 4.2 Å along the trajectories. The representative structures A-F, as depicted in Fig. 3, highlight the dynamic nature of the π-π interactions, showcasing a variety of conformations. Using a 4.2 Å cut-off value, $\mathbf{R_{3F}}$ exhibits π-π interactions in 97 % of conformations, while $\mathbf{R_{2F}}$ shows 77 %, aligning with our observations from both simulated trajectories and NMR experiments. To delve into further details of their conformations, clustering analyses were performed. The pronounced tendency to form π-π interactions in $\mathbf{R_{2F}}$ and $\mathbf{R_{3F}}$ impedes the wheel's conformational transition, leading to proton splitting. Without the steric hindrance of the second wheel, $\mathbf{R_{2F}}$ displays a higher propensity to exist without any π-π interaction, resembling conformer A, compared to $\mathbf{R_{3F}}$ (23 % versus 3 %). Conversely, the second wheel in $\mathbf{R_{3F}}$ promotes the formation of π-π interactions, akin to the "double-wave"-shaped conformer E proposed by ^{1}H NMR, which minimizes steric hindrance between the wheels. However, driven by the π-π interaction, $\mathbf{R_{3F}}$ can even adopt a "big-wave"-shaped conformer F with the adjacency of four perfluoro-*tert*-butyl groups. Additionally, due to the twisted "Z" conformation of the two wheels, they are very likely unable to move independently but instead exhibit a concerted movement within $\mathbf{R_{3F}}$. In all, MD simulations underscore a strong tendency to form π-π interactions between the wheel and the axle, elucidating the pivotal role of π-π interaction in the molecular dynamics of $\mathbf{R_{3F}}$. Notably, the simulated video (available in the Supporting Information) of the rotaxanes corroborates similar MDs as proposed by ^{1}H/^{19}F NMR.

After uncovering the internal factors shaping the MD of rotaxanes, we delved into the influence of external factors. Initially, we explored the impact of temperature variation on crowded $\mathbf{R_{3F}}$ and loose $\mathbf{R_F}$. Increasing the temperature from 274 K to 315 K revealed a more pronounced decrease in the relaxation rates of wheel fluorines in $\mathbf{R_F}$ compared to $\mathbf{R_{3F}}$ (Fig. 4a). This observation suggests that the energy input stimulated greater motion of the wheels in the loose rotaxanes. In the absence of steric hindrance, the energy input predominantly enhances wheel motion in $\mathbf{R_F}$, potentially expediting conformational transitions and spin movement. Subsequently, we investigated the effect of solvent viscosity by transitioning from methanol to 1-butanol. Despite varying solvent viscosities (η, methanol: 0.54, ethanol: 1.08, 1-propanol: 1.95, 1-butanol: 2.59), no significant difference in the relaxation rate

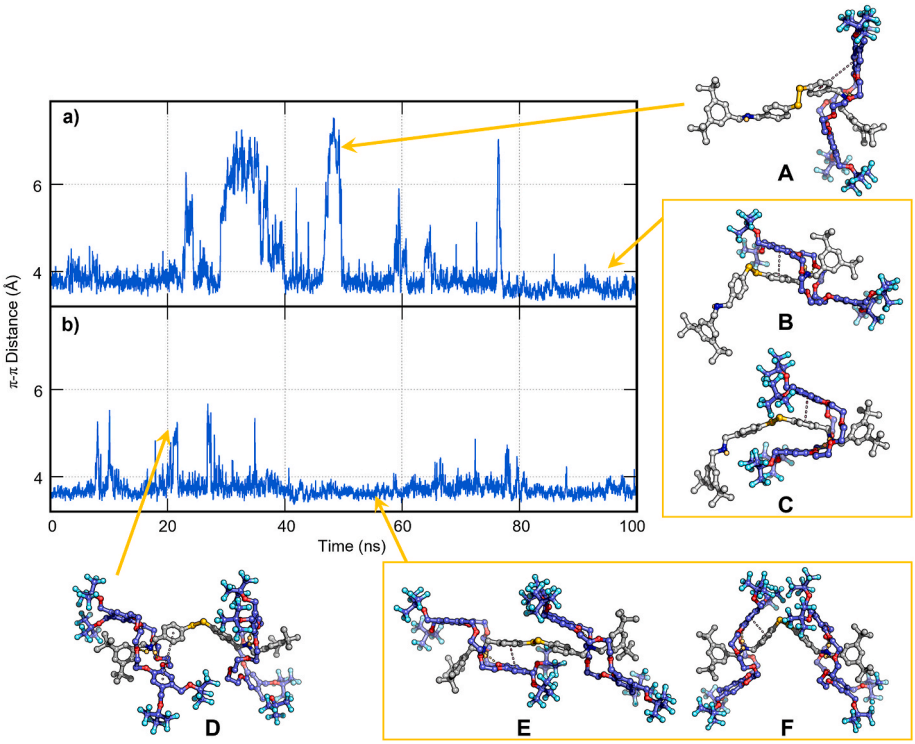

Fig. 3. One of the simulated trajectories of $\mathbf{R_{2F}}$ (a) and $\mathbf{R_{3F}}$ (b) by the minimum π-π distance along the time with their representative conformations.

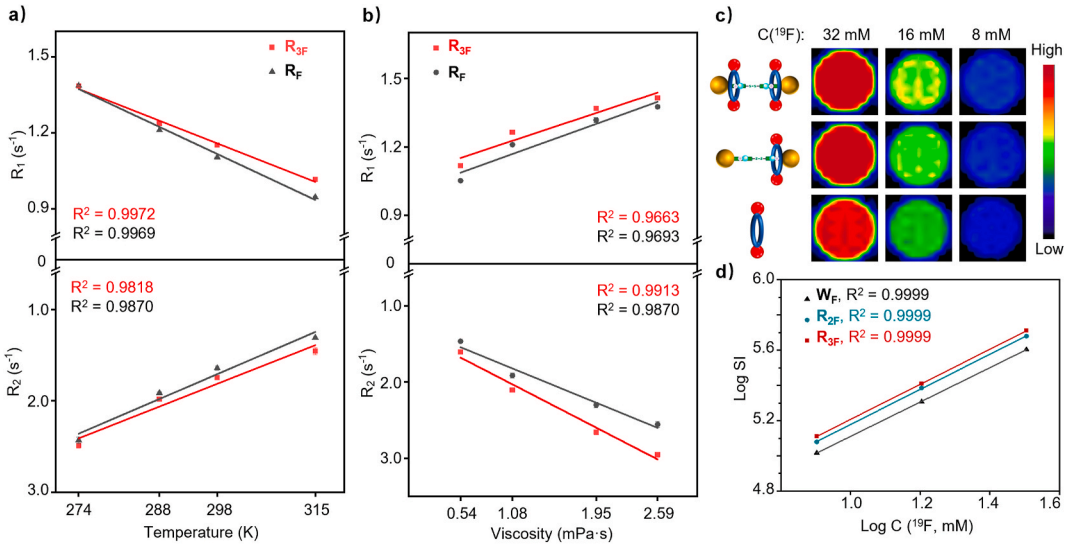

Fig. 4. Temperature-dependent (a) and viscosity-dependent (b) wheel fluorines relaxation rates of $\mathbf{R_F}$ and $\mathbf{R_{3F}}$. ^{19}F MRI phantom images (c, 9.4 T, 298 K, CH_3CN) and the plot of LogSI versus LogC (^{19}F) (d) of $\mathbf{W_F}$, $\mathbf{R_{2F}}$, and $\mathbf{R_{3F}}$. SI represents signal intensity.

increases of wheel fluorines was noted in $\mathbf{R_{3F}}$ and $\mathbf{R_F}$ (Fig. 4b). This finding suggests that the viscous solvent impedes the motion of the entire molecules regardless of molecular size and structure. Hence, the motion of wheels in rotaxanes can be modulated by both energy input and solvent viscosity, offering potential avenues for triggering novel functionalities in rotaxane-based molecular devices.

Finally, ^{19}F MRI was leveraged to detect changes in molecular dynamics among $\mathbf{W_F}$, $\mathbf{R_{2F}}$, and $\mathbf{R_{3F}}$. In longitudinal relaxation time (T_1, $T_1 = 1/R_1$)-weighted ^{19}F MRI, a compound with shorter T_1 enables faster data acquisition and yields higher signal intensity within a given time [34]. Threading $\mathbf{W_F}$ into $\mathbf{R_{2F}}$ led to a 23 % reduction in T_1, while threading two $\mathbf{W_F}$ into $\mathbf{R_{3F}}$ resulted in a 28 % reduction, sensitively detected by the enhancement of ^{19}F MRI signal intensity on T_1-weighted ^{19}F MRI at identical fluorine concentrations (Fig. 4c). At a fluorine concentration of 16 mM, the threading of $\mathbf{W_F}$ into $\mathbf{R_{2F}}$ induced a 20 % enhancement in ^{19}F MRI signal intensity, underscoring the impact of mechanical bond, hydrogen bonding, and π-π interaction between the perfluoro-*tert*-butyl and *tert*-butyl groups. Meanwhile, the addition of an extra wheel into $\mathbf{R_{3F}}$ resulted in a 27 % enhancement in ^{19}F MRI signal intensity, representing the influence of steric hindrance. These subtle alterations in molecular dynamics are perceptible in ^{19}F MRI with the naked eye. In each scenario, the logarithm of ^{19}F MRI signal intensity is directly proportional to the logarithm of fluorine concentration (Fig. 4d), facilitating precise quantification of $\mathbf{W_F}$, $\mathbf{R_{2F}}$, and $\mathbf{R_{3F}}$ with ^{19}F MRI signal intensity. Consequently, the molecular dynamics of rotaxanes were effectively assessed via ^{19}F MRI, distinctly illustrating the impacts of mechanical bond and steric hindrance on molecular dynamics.

4. Conclusion

In summary, we have introduced a series of innovative fluorinated rotaxanes equipped with dynamic, sensitive, selective, and semi-quantitative ^{1}H/^{19}F NMR status reporters for tracking molecular dynamics. By dissecting the "double wave" structure of [3]rotaxanes through 1D and 2D ^{1}H/^{19}F NMR spectra, we successfully utilized the ^{1}H/^{19}F relaxation rates of these reporters to explore the influence of both internal factors (mechanical bond, hydrogen bond, π-π interaction, steric hindrance, and molecular weight) and external factors (temperature and solvent viscosity) on molecular dynamics in a comparative manner. Our investigations revealed that, beyond the mechanical bond, steric hindrance significantly modulates the motion of adjacent axle groups and the conformational transition of the wheel, with molecular dynamics simulations shedding further light on the role of π-π interaction. Contrasting conventional spectroscopy and imaging techniques used for monitoring rotaxanes, ^{19}F NMR/MRI offers distinct and complementary structural and dynamic insights through parameters such as the ^{19}F signal (shape, shift), relaxation rates, rotational correlation time, and imaging features (signal intensity, spatial distribution). Importantly, the background-free ^{19}F NMR/MRI signals provide quantitative information for selective monitoring of molecular dynamics in complex systems, including those with multiple components and intricate supramolecular interactions, as well as under biological conditions. Overall, our successful implementation of ^{19}F magnetic resonance spectroscopy and imaging technologies enables sensitive and semi-quantitative tracking of molecular dynamics in rotaxanes, thereby enhancing our understanding, rational design, and application of molecular devices. We are currently pursuing the synthesis and application of other fluorinated molecular devices, with results forthcoming in due course.

CRediT authorship contribution statement

Yu Li: Writing – review & editing, Investigation, Formal analysis. **Man Luo:** Investigation, Formal analysis. **Mou Jiang:** Investigation, Formal analysis. **Rui Zhou:** Formal analysis. **Wanrong Yang:** Investigation. **Shenhui Li:** Investigation. **Fang Wang:** Writing – review & editing, Funding acquisition. **Lijun Zhu:** Writing – review & editing. **Pei He:** Writing – review & editing. **Minghui Yang:** Formal analysis. **Xin Zhou:** Supervision, Funding acquisition. **Zhong-Xing Jiang:** Writing – review & editing, Writing – original draft, Funding acquisition, Conceptualization. **Shizhen Chen:** Supervision, Funding acquisition, Conceptualization.

Declaration of competing interest

The authors declare that they have no known competing financial interests or personal relationships that could have appeared to influence the work reported in this paper.

Data availability

Data will be made available on request.

Acknowledgements

This work was supported by the Strategic Priority Research Program of the Chinese Academy of Sciences (XDB0540000), the National Key R&D Program of China, China (2018YFA0704000), the National Natural Science Foundation of China (22327901, 22077098, U21A20392, 21921004, and 82127802), the China Postdoctoral Science Foundation (2023M743583 and GZC20232754), the Knowledge Innovation Program of Wuhan-Basic Research (2022020801010137), and the Youth Innovation Promotion Association, China and the Young Top-notch Talent Cultivation.

Appendix A. Supplementary data

Supplementary data to this article can be found online at https://doi.org/10.1016/j.aca.2024.342983.

References

[1] J.F. Stoddart, The chemistry of the mechanical bond, Chem. Soc. Rev. 38 (2009) 1802–1820.
[2] V. Serreli, C.-F. Lee, E.R. Kay, D.A. Leigh, A molecular information ratchet, Nature 445 (2007) 523–527.
[3] M. Xue, Y. Yang, X. Chi, X. Yan, F. Huang, Development of pseudorotaxanes and rotaxanes: from synthesis to stimuli-responsive motions to applications, Chem. Rev. 115 (2015) 7398–7501.
[4] W.-J. Li, Z. Hu, L. Xu, X.-Q. Wang, W. Wang, G.-Q. Yin, D.-Y. Zhang, Z. Sun, X. Li, H. Sun, H.-B. Yang, Rotaxane-branched dendrimers with enhanced photosensitization, J. Am. Chem. Soc. 142 (2020) 16748–16756.
[5] W.-J. Li, Q. Gu, X.-Q. Wang, D.-Y. Zhang, Y.-T. Wang, X. He, W. Wang, H.-B. Yang, AIE-active chiral [3]rotaxanes with switchable circularly polarized luminescence, Angew. Chem. Int. Ed. 60 (2021) 9507–9515.
[6] E. Kolodzeiski, S. Amirjalayer, Dynamic network of intermolecular interactions in metal-organic frameworks functionalized by molecular machines, Sci. Adv. 8 (2022) eabn4426.
[7] X. Yang, L. Cheng, Z. Zhang, J. Zhao, R. Bai, Z. Guo, W. Yu, X. Yan, Amplification of integrated microscopic motions of high-density [2]rotaxanes in mechanically interlocked networks, Nat. Commun. 13 (2022) 6654.
[8] J.F. Stoddart, The chemistry of the mechanical bond, Chem. Soc. Rev. 38 (2009) 1802–1820.
[9] S. Chen, D. Su, C. Jia, Y. Li, X. Li, X. Guo, D.A. Leigh, L. Zhang, Real-time observation of the dynamics of an individual rotaxane molecular shuttle using a single-molecule junction, Chem 8 (2022) 243–252.
[10] Y. Yasuda, M. Toda, K. Mayumi, H. Yokoyama, H. Morita, K. Ito, Sliding dynamics of ring on polymer in rotaxane: a coarse-grained molecular dynamics simulation study, Macromolecules 52 (2019) 3787–3793.
[11] L. Leanza, C. Perego, L. Pesce, M. Salvalaglio, M. von Delius, G.M. Pavan, Into the dynamics of rotaxanes at atomistic resolution, Chem. Sci. 14 (2023) 6716–6729.
[12] Q.-W. Zhang, J. Zajíček, B.D. Smith, Cyclodextrin rotaxane with switchable pirouetting, Org. Lett. 20 (2018) 2096–2099.
[13] P. Liu, X. Shao, C. Chipot, W. Cai, The true nature of rotary movements in rotaxanes, Chem. Sci. 7 (2016) 457–462.
[14] K. Zhu, G. Baggi, S.J. Loeb, Ring-through-ring molecular shuttling in a saturated [3]rotaxane, Nat. Chem. 10 (2018) 625–630.
[15] Y. Kawasaki, S. Rashid, K. Ikeyatsu, Y. Mutoh, Y. Yoshigoe, S. Kikkawa, I. Azumaya, S. Hosoya, S. Saito, Conformational control of [2]rotaxane by hydrogen bond, J. Org. Chem. 87 (2022) 5744–5759.
[16] G. Jana, J.L. Mendoza-Cortes, Thermodynamics, kinetics, and optical properties of rotaxane: a first-principles molecular dynamics study, J. Phys. Chem. A 127 (2023) 2671–2687.
[17] J.W. Peng, Exposing the moving parts of proteins with NMR spectroscopy, J. Phys. Chem. Lett. 3 (2012) 1039–1051.
[18] S. Stoffel, Q.-W. Zhang, D.-H. Li, B.D. Smith, J.W. Peng, NMR relaxation dispersion reveals macrocycle breathing dynamics in a cyclodextrin-based rotaxane, J. Am. Chem. Soc. 142 (2020) 7413–7424.
[19] D. Kumar, Y. Krishnan, M. Paranjothy, S. Pal, Determination of inclusion geometry of cyclodextrin host-guest complexes: applicability of 1D selective NMR methods, J. Magn. Reson. Open 10–11 (2022) 100053.
[20] J. Ruiz-Cabello, B.P. Barnett, P.A. Bottomley, J.W.M. Bulte, Fluorine (F) MRS and MRI in biomedicine, NMR Biomed. 24 (2011) 114–129.
[21] I. Tirotta, V. Dichiarante, C. Pigliacelli, G. Cavallo, G. Terraneo, F.B. Bombelli, P. Metrangolo, G. Resnati, ^{19}F magnetic resonance imaging (MRI): from design of materials to clinical applications, Chem. Rev. 115 (2015) 1106–1129.
[22] T. Wu, A. Li, K. Chen, X. Peng, J. Zhang, M. Jiang, S. Chen, X. Zheng, X. Zhou, Z.-X. Jiang, Perfluoro-tert-butanol: a cornerstone for high performance fluorine-19 magnetic resonance imaging, Chem. Commun. 57 (2021) 7743–7757.
[23] S. Rashid, T. Murakami, H. Koganezawa, Y. Yoshigoe, S. Hosoya, S. Saito, Fluorinated [2]rotaxanes with spirofluorene motifs: a non-symmetric distribution of the ring component along the axle component, New J. Chem. 47 (2023) 900–909.
[24] B.E. Fletcher, M.J.G. Peach, N.H. Evans, Rapidly accessible “click” rotaxanes utilizing a single amide hydrogen bond templating motif, Org. Biomol. Chem. 15 (2017) 2797–2803.
[25] M.J. Power, D.T.J. Morris, I.J. Vitorica-Yrezabal, D.A. Leigh, Compact rotaxane superbases, J. Am. Chem. Soc. 145 (2023) 8593–8599.
[26] L. Yang, Y. Li, M. Jiang, R. Zhou, H. Cong, M. Yang, L. Zhang, S. Li, Y. Yang, M. Liu, X. Zhou, Z.-X. Jiang, S. Chen, Fluorinated [2]rotaxanes as sensitive ^{19}F MRI agents: threading for higher sensitivity, Chin. Chem. Lett. (2024) 109512.
[27] T. Yoshii, Y. Kohsaka, T. Moriyama, T. Suzuki, Y. Koyama, T. Takata, An efficient synthetic entry to rotaxanes utilising reversible cleavage of aromatic disulphide bonds, Supramol. Chem. 23 (2011) 65–68.
[28] K.D. Hänni, D.A. Leigh, The application of CuAAC ‘click’ chemistry to catenane and rotaxane synthesis, Chem. Soc. Rev. 39 (2010) 1240–1251.
[29] A. Swartjes, P.B. White, J.P.J. Bruekers, J.A.A.W. Elemans, R.J.M. Nolte, Paramagnetic relaxation enhancement NMR as a tool to probe guest binding and exchange in metallohosts, Nat. Commun. 13 (2022) 1846.
[30] C. Dalvit, M. Veronesi, A. Vulpetti, ^{1}H and ^{19}F NMR chemical shifts for hydrogen bond strength determination: correlations between experimental and computed values, J. Magn. Reson. Open 12–13 (2022) 100070.
[31] M. Taguchi, N. Suzuki, M. Fujiki, Intramolecular CH/π interaction of Poly(9,9-dialkylfluorene)s in solutions: interplay of the fluorene ring and alkyl side chains revealed by 2D ^{1}H–^{1}H NOESY NMR and 1D ^{1}H-NMR experiments, Polym. J. 45 (2013) 1047–1057.
[32] R. Kubo, K. Tomita, General theory of magnetic resonance absorption, J. Phys. Soc. Jpn. 9 (1954) 888–919.
[33] R. Salomon-Ferrer, A.W. Götz, D. Poole, S. Le Grand, R.C. Walker, Routine microsecond molecular dynamics simulations with AMBER on GPUs. 2. explicit solvent particle mesh ewald, J. Chem. Theor. Comput. 9 (2013) 3878–3888.
[34] A.A. Kislukhin, H. Xu, S.R. Adams, K.H. Narsinh, R.Y. Tsien, E.T. Ahrens, Paramagnetic fluorinated nanoemulsions for sensitive cellular fluorine-19 magnetic resonance imaging, Nat. Mater. 15 (2016) 662–668.